Received: 31 March 2023 | Revised: 14 May 2023 | Accepted: 16 May 2023

DOI: 10.1002/jcc.27168

RESEARCH ARTICLE

Journal of Computational Chemistry WILEY

# Chemical bonding of HF, HCl, and $H_2O$ onto $YF_3$ surfaces: Quantification by first principles

Jennifer Anders[1] | Henrik Wiedenhaupt[1] | Florian Kreuter[2] | Ralf Tonner-Zech[2] | Beate Paulus[1]

[1]Institut für Chemie und Biochemie, Freie Universität Berlin, Berlin, Germany

[2]Wilhelm-Ostwald-Institut für Physikalische und Theoretische Chemie, Universität Leipzig, Leipzig, Germany

**Correspondence**
Jennifer Anders, Institut für Chemie und Biochemie, Freie Universität Berlin, Arnimallee 22, 14195 Berlin, Germany.
Email: jennifer.anders@fu-berlin.de

**Funding information**
Deutsche Forschungsgemeinschaft

## Abstract

The surfaces of waimirite β-$YF_3$have been studied for their fluorine and chlorine versus water affinity. Bonding patterns of HF, HCl, and $H_2O$ chemically adsorbed onto surfaces of (010), (100), (011), and (101) have been quantified by density functional theory applying energy decomposition analysis. We found that the adsorption of $H_2O$ is dominated by about 65% of electrostatics, which causes a low surface sensitivity and weak interactions. On the contrary, the adsorptions of HF and HCl are driven by strong hydrogen bonds resulting in a highly surface-dependent ratio of 30–60% electrostatic versus orbital contribution. Among the stoichiometric surfaces, the shortest and strongest hydrogen bonds and consequently most covalent bonding patterns are found within $YF_3$·HCl. However, when including the preparation energy, each surface favors the adsorption of HF over HCl, which reproduces the higher affinity of yttrium towards fluoride over chloride, previously known for solutions, also for the solid state.

**KEYWORDS**
DFT, HFSE, pEDA, surface adsorption, waimirite

## 1 | INTRODUCTION

Current research suggests that subtle differences within the fluoride and chloride affinities of solvated rare earth element or yttrium (REE+Y) cations have a major impact on their hydrothermal transport.[1-8] However, little is known how these translate to the solid phase and which impact the surface structure has. The prototype structure for most REE+Y fluorides is β-$YF_3$, an interesting host material for laser applications due to its huge absorption-free window.[9-15] Moreover, by its extraordinary high $F^-$ conductivity, it is a promising candidate for the upcoming field of solid state fluoride batteries.[16-20] In nature, β-$YF_3$ is found as the mineral waimirite-(Y).[9] Ore forming and enriching processes are generally dominated by simple electrostatics driven by ionic radius and charge.[2] The ionic radius of 107.5 pm found for Y(III) is well within the range of middle to late lanthanides of samarium(III)–lutetium(III).[21] Consequently, these are found in relatively high concentrations within waimirite.[9] Nevertheless, as Y is 4–74 times more abundant within the upper continental Earth's crust than Sm–Lu, it remains the dominant cation within the lattice.[22,23] The accumulation of REE within ores in general, as well as the enrichment of other high field strength elements (HFSE) is reasoned to be mainly driven by fluoride, because of the stronger complexes formed than with chloride.[1,2,4,24-26] This is especially pronounced for the later lanthanides, due to their smaller ionic radii and thus even harder ionic character.[27] Ab initio molecular dynamics (AIMD) simulations of Y(III) in aqueous solutions of 1 molal NaCl and 0.0001–0.1 molal NaF have shown a clear preference for fluoride. For concentrations below 0.01 molal NaF, $YCl_2^+$ has been found the dominant Y-species.

However, above that threshold, $YF_3$ has been predicted the most dominant Y-species, despite the still 100 times higher availability of chloride.[5] The difference in affinity for chloride and fluoride shown by the HFSE can already be qualitatively predicted by electrostatics, only, or the simple concept of hard and soft Lewis acids and bases (HSAB). However, electrostatics alone cannot predict that two cations of equivalent charge to radius ratio show a different affinity for the same anion. However, such fluoro-specific interactions have been found within dissolving measurements of solid β-$YF_3$ and β-$HoF_3$ in aqueous HF (0.001–0.3 molal), which revealed that both equally sized cations form different fluoride-species of $YF_2^+$ and $HoF^{2+}$ in solution.[4] This difference in fluoride affinity can only occur if besides simple electrostatics, the different nature of their occupied orbitals plays a role. It is not possible to directly access the energy of electrostatics versus orbital contributions, as well as bonding patterns of hydrogen bonds (H-bonds) by experiments. Consequently, this gap may be ideally filled by computational insights. To illuminate, whether this preference for fluoride over chloride is also present in the solid state, and especially, if this applies to all surface cuts, we invest adsorptions of HF, HCl, or $H_2O$ onto several pristine β-$YF_3$ surfaces. By this simplistic model system, we aim to quantify the difference in affinity between chloride and fluoride in reference to water, explore how large the ratios of electrostatics versus orbital contributions vary, which bonding patterns are inherent to these, and to which degree they depend on the chosen surface.

## 2 | METHODOLOGY

### 2.1 | $YF_3$ structure and surfaces

Below temperatures of 1350 K, $YF_3$ crystallizes in its orthorhombic β-phase.[15,28] The *Pnma*-symmetric unit cell (see Figure 1) is constituted by four formula units of $YF_3$ fully occupying the Wyckoff positions 4c (Y), 4c (F), and 8d (F).

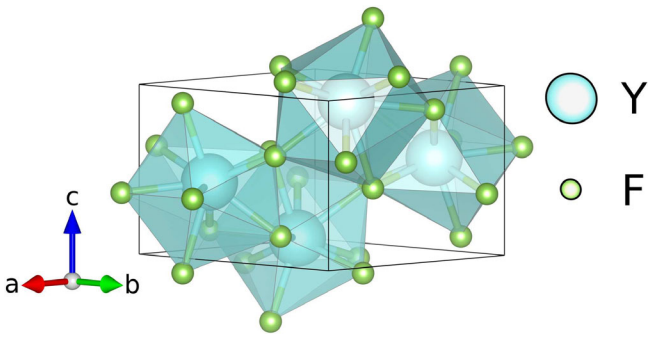


**FIGURE 1** Unit cell of β-$YF_3$ with (PBE) relaxed lattice parameters of $a = 6.3215$ Å, $b = 6.8059$ Å, and $c = 4.3300$ Å.[29] Each unit cell contains four F bridging two Y and eight F coordinating to three Y. All Y are symmetry-equivalent, each coordinated by nine F forming a distorted tricapped trigonal anti-prism.

Within a previous study, the surface formation energies ($E_{surf}$) have been calculated from the difference in total energies of the slab supercell ($E_n$) and the bulk unit cell ($E_{bulk}$) multiplied by the number of unit cells within the slab ($n$).[29] This difference has been divided by double the surface area ($A$) as symmetric slabs have been used.

$$E_{surf} = \frac{E_n - nE_{bulk}}{2A} \tag{1}$$

For the substoichiometric surface of (101), the F potential ($\mu_F$) is added to the numerator for each missing F. $\mu_F$ itself has been derived from the unit cells of $YF_3$ and metallic Y. Applying a Wulff analysis on these energies, we found the following abundances for the different low-lying Miller indices surfaces (*hkl*): 26% (010), 22% (011), 20% (101), 10% (001), 10% (111), 7% (100), and 5% (110).[29-31] The two most available surfaces, (010) and (011) possess terminations that are stoichiometric, whereas the third most abundant surface (101) prefers a substoichiometric termination missing one surface fluorine atom ($F_{surf}$) per four surface yttrium atoms ($Y_{surf}$). Together, these three surfaces constitute 68% of the overall crystalline surface. Additionally, we also include the lesser abundant stoichiometric surface (100) to compare to future studies on $HoF_3$ surface, as in contrast to $YF_3$, it is with 25% the second most available surface in $HoF_3$. All four surfaces cover 75% of the $YF_3$ crystal. Within the bare relaxed surface supercells, (010) only contains eight-fold coordinated $Y_{surf}$ (see Figure 2). (100) and (011) show six- and nine-fold coordinations, in which the six-fold coordination of (100) leaves the $Y_{surf}$ more exposed. The substoichiometric (101) contains $Y_{surf}$ in six-, seven-, and eight-fold coordination. These six-fold coordination polyhedra leave the $Y_{surf}$ much more accessible, than in the other surfaces. Thus, the accessibility of $Y_{surf}$ increases as (010) < (011) < (100) < (101).

### 2.2 | Approach to model adsorptions

The studied adsorption structures originate from scanning the conformational landscape of HF and $H_2O$ adsorptions onto the three most stable $YF_3$ surfaces of (010), (011), and (101) done in a preceding study.[32] It covered 200 ps of AIMD simulations, as well as over 300 systematically created, differently orientated monolayers of adsorbate molecules. From these, coordinations of single or multiple molecules have been extracted. The lesser stable surface of (100) was not part of this conformational scan. Instead, the (100)·Ads (Ads = $H_2O$, HF, HCl) structures have been obtained by transferring adsorbate coordinations from other surfaces. Moreover, all single HCl adsorptions of $YF_3$·HCl originate from the respective $YF_3$·HF structures. From all $YF_3$·Ads structures, 38 chemically nonequivalent single adsorbate structural isomers (grouped form 46 relaxed structures) and 8 multiple adsorbate structural isomers are considered within this work. These are visualized in Figures S5–S17. Their adsorption energies are split into their subcomponents yielding insight into their

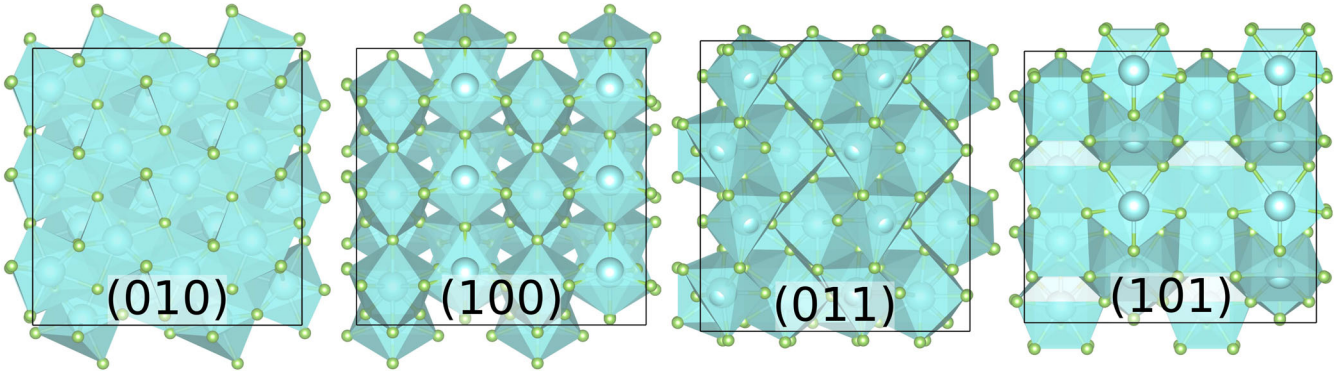


**FIGURE 2** Topview onto the bare surface supercells of (4 × 3 × 4) $YF_3$-layers for (010) and (100) or (4 × 4 × 4) $YF_3$-layers for (011) and (101), each with the top two layers (PBE+D3(BJ)) relaxed.

covalent versus ionic character. This also allows to quantify the contributions of H-bond to $F_{surf}$ versus direct coordination to $Y_{surf}$. This division is done with the pEDA with NOCV extension method as implemented in AMS-BAND and described below. However, for periodic systems, a plane waves basis set as used in VASP is much more efficient than an atom-centered one, especially if these are Slater-type orbitals as in AMS-BAND. Therefore, all atomic coordinates are kept as relaxed inside VASP and only the electronic structure is recalculated inside AMS-BAND. We validated this approach by calculating the bonding energy with relaxed reactants ($\Delta E_{bond}$) for all (010)·$(Ads)_n$ according to Reaction R1. We found an excellent agreement ($R^2 = 0.9999$, $\Delta\Delta E_{bond} \leq 2$ kJ mol$^{-1}$ per adsorbate molecule) between $\Delta E_{bond}$ determined purely within VASP and by recalculating the electronic energies within AMS-BAND (see Figures S3 and S4). For the other stoichiometric surfaces of (100) and (011) showing stronger adsorptions, $\Delta\Delta E_{bond}$ remains almost identical with ≤ 3 kJ smol$^{-1}$ (see Table 2). For substoichiometric (101), the difference grows to ≤ 5 kJ mol$^{-1}$, however, given the much larger absolute values, these are just ≤ 1.6%.

## 2.3 | Quantifying adsorption by pEDA with NOCV extension

Within this paper, we quantified the electronic adsorption energies of different adsorbates (Ads) onto different surfaces of $YF_3$. The adsorption energy with relaxed atomic structures (superscript 0) of reactants and product according to Reaction R1 is referred to as bonding energy ($\Delta E_{bond}$). For $\Delta E_{bond}$ with multiple molecules adsorbed, a multiple of the isolated molecule was taken.

$$YF^0_{3(surf)} + n\ Ads^0_{(gas)} \xrightarrow{\Delta E_{bond}} YF_3 \cdot (Ads)^0_{n(surf)} \quad (R1)$$

In contrast, the interaction energy ($\Delta E_{int}$) refers to the adsorption energy obtained from reactants with the same atomic structure as inside the product (see Reaction R2).

$$YF_{3(surf)} + (Ads)_{n(gas)} \xrightarrow{\Delta E_{int}} YF_3 \cdot (Ads)^0_{n(surf)} \quad (R2)$$

Therefore both adsorption energies differ by the relaxation (or preparation) of the reactants ($\Delta E_{prep}$).

$$\Delta E_{bond} = \Delta E_{prep} + \Delta E_{int} \quad (2)$$

Using a PBE+D3 approach,[33] the energy attributed to dispersion interaction ($\Delta E_{disp}$) may be separated from $\Delta E_{int}$ leaving an electronic term ($\Delta E_{int}$(elec)) associated with covalent bonding.

$$\Delta E_{int} = \Delta E_{disp} + \Delta E_{int}(elec) \quad (3)$$

By periodic energy decomposition analysis (pEDA), $\Delta E_{int}$(elec) can be separated further into its subcontributions of semi-classical electrostatics ($\Delta E_{elstat}$), as well as attractive orbital contributions ($\Delta E_{orb}$), and a repulsive term to account for the Pauli principle ($\Delta E_{Pauli}$).[34-36]

$$\Delta E_{int}(elec) = \Delta E_{elstat} + \Delta E_{orb} + \Delta E_{Pauli} \quad (4)$$

The first two terms of Equation (4) may be combined to the attractive interaction ($\Delta E_{attr}$).

$$\Delta E_{attr} = \Delta E_{elstat} + \Delta E_{orb} \quad (5)$$

Finally, $\Delta E_{orb}$ is split into pairwise orbital interactions of natural orbitals for chemical valence (NOCV) between the surface and the adsorbate.[37,38] The NOCVs are the eigenvectors of the deformation density matrix, which is the density difference between the intermediate and the final state in the EDA procedure. The corresponding eigenvalues are a qualitative measure of the amount of charge transferred.

## 2.4 | Computational details

All atomic structures within this study have been partially (adsorbates and top two $YF_3$-layers) relaxed. These originate from our preceding

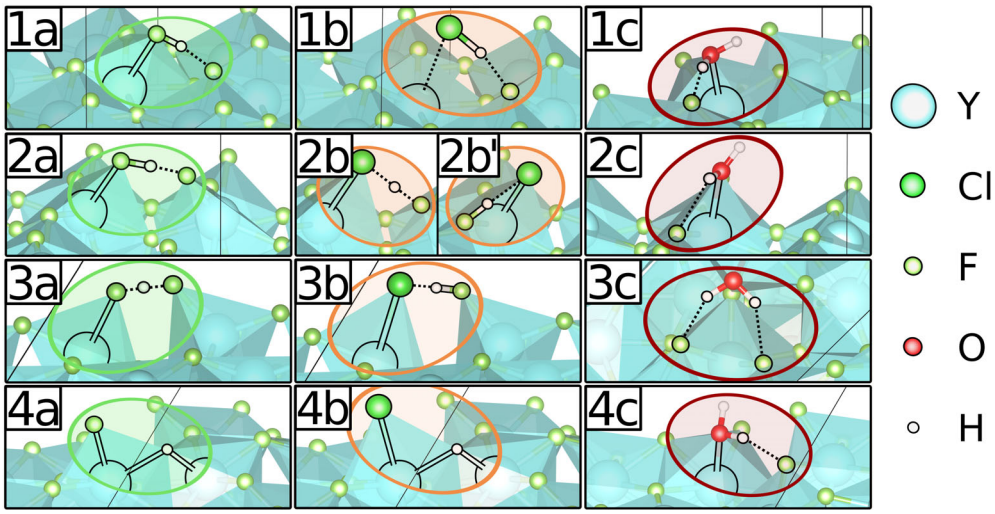


**FIGURE 3** Atomic structures of the respective strongest adsorptions of $YF_3$·HF (**1**–**4a**), $YF_3$·HCl (**1**–**4b**), and $YF_3 \cdot H_2O$ (**1**–**4c**) onto (010) (**1a**–**c**), (100) (**2a**–**c**), (011) (**3a**–**c**), or (101) (**4a**–**c**).

**TABLE 1** Comparison of studied surfaces ordered according to their $Y_{surf}$ accessibility listing their surface energies ($E_{surf}$; PBE) and ratios ($\%_{surf}$)[29] with the respective strongest bound $YF_3$·Ads (see Figure 3; PBE+D3(BJ)) yielding the strongest interaction ($\Delta E_{int}$), as well as bonding energy ($\Delta E_{bond}$); for (100)·HCl, these are obtained by two different structures giving the one with the strongest $\Delta E_{int}$ (**2b'**) in parenthesis; the coordination numbers ($CN^{Y}_{surf}$) correspond to the empty adsorption site $Y_{surf}$ of the bare surface.

| (*hkl*) | $E_{surf}$ in J·m$^{-2}$ | $\%_{surf}$ in % | $CN^{Y}_{surf}$ HF/HCl | $CN^{Y}_{surf}$ $H_2O$ | $\lvert\Delta E_{int}\rvert$ in kJ mol$^{-1}$ HF | $\lvert\Delta E_{int}\rvert$ HCl | $\lvert\Delta E_{int}\rvert$ $H_2O$ | $\lvert\Delta E_{bond}\rvert$ in kJ mol$^{-1}$ HF | $\lvert\Delta E_{bond}\rvert$ HCl | $\lvert\Delta E_{bond}\rvert$ $H_2O$ |
|---|---|---|---|---|---|---|---|---|---|---|
| (010) | 0.58 | 26 | 8 | 8 | 106 | 57 | 104 | 75 | 42 | 86 |
| (011) | 0.61 | 22 | 6 | 6 | 253 | 265 | 135 | 123 | 90 | 114 |
| (100) | 1.03 | 7 | 6 | 6 | 194 | 227 (376) | 102 | 134 | 97 (83) | 93 |
| (101) | 0.76 | 20 | 6 | 8 | 969 | 821 | 130 | 310 | 306 | 111 |

work on $YF_3$ surface adsorptions[32] done within the Vienna Ab Initio Simulation Package (VASP, version 5.4.4)[39] applying the computational setup showing very good agreement with the crystal unit cell.[29] Summing up, the Perdew–Burke–Ernzerhof (PBE) functional[40] with the projector augmented wave (PAW) method[41,42] with a kinetic cutoff of 772.6 eV using the soft valence Y, as well as the hard H, O, F, and Cl core PAW potentials yielding respective valence electron numbers of 11, 1, 6, 7, and 7. The previously tested effect of normal versus hard core potentials showed a better description using the latter, especially for HF.[32] Around the isolated molecules and perpendicular to the surface plane, 25 Å vacuum has been applied as converged in our previous $YF_3$ study.[29] A neglectable adsorbate-adsorbate interaction using the Γ-point only was found at supercell sizes of $(4 \times 3 \times 4)$ $YF_3$-layers for (010) and (100) or $(4 \times 4 \times 4)$ $YF_3$-layers for (101) and (011) with respective surface areas of 164 Å$^2$ (010), 177 Å$^2$ (100), 204 Å$^2$ (011) or 209 Å$^2$ (101).[32] These are visualized in Figure 2. The adsorbate molecules and the first two $YF_3$-layers of each surface have been relaxed in atomic coordinates with allowed spin polarization, Gaussian smearing with a width of 0.2 eV and Grimme's dispersion correction with Becke-Johnson damping (D3(BJ)).[33,43] For the bare surfaces, the first two layers consist of 48 atoms for (010) and (100) or 64 atoms for (101) and (011). The atomic structure relaxations performed inside VASP have been done with an energetic atomic relaxation criterion of $10^{-4}$ eV between two ionic steps and a self-consistent field (SCF) convergence criterion of $10^{-5}$ eV. Final electronic structures have been calculated with a SCF criterion of $10^{-6}$ eV. Onto all VASP calculations, a self-consistent field (SCF) convergence criteria of $10^{-5}$ eV for atomic structure relaxations and $10^{-6}$ eV for the final electronic structure have been applied.

VASP-derived energies ($E^{VASP}$) given are labeled accordingly. All energies without superscript label originate from PBE+D3 (BJ) electronic energies by AMS-BAND version 2021.102.[44] Frozen core sizes have been chosen to obtain the same number of valence electrons as within VASP. This corresponds to a large frozen core on Cl and small frozen cores on O, F, and Y. Tests of applying the default, large frozen core on Y yielded unsatisfactory results (see Figure S1 and Table S1 ). The effects of basis set, *k*-grid and numerical quality were tested (see SI Section 1). These tests yielded TZ2P at the Γ-point only with a very good numerical quality as the best setup. The letter corresponds to a SCF criterion of at least $1.6 \times 10^{-7}$ eV. Scalar relativistic effects were treated by the zeroth order regular approximation (ZORA).[45,46] All systems that converged

**TABLE 2** Energy contributions (PBE+D3(BJ)) to $\Delta E_{bond}$ in kJ mol$^{-1}$ with $\Delta E_{int}$ ($\Delta E_{disp}$, $\Delta E_{elstat}$, $\Delta E_{orb}$, $\Delta E_{Pauli}$) and $\Delta E_{prep}$ of the adsorbate and surface of the strongest adsorbed $YF_3$·Ads with percentages among $\Delta E_{attr}$ (%$_a$) or $\Delta E_{int}$ (%$_i$) given in parenthesis; for (100)·HCl, both strongest adsorptions are listed in order of strongest by $\Delta E_{bond}$ (**2b**) or $\Delta E_{int}$ (**2b'**); the VASP-derived $\Delta E_{bond}^{VASP}$ as in Reference 32 are given for comparison.

| HF | (010) | (100) | (011) | (101) |
|---|---|---|---|---|
| $\Delta E_{bond}^{VASP}$ | −75 | −135 | −125 | −315 |
| $\Delta E_{bond}$ | −75 | −134 | −123 | −310 |
| $\Delta E_{int}$ | −106 | −194 | −253 | −969 |
| $\Delta E_{disp}$ | −12 (11%$_i$) | −9 (5%$_i$) | −9 (4%$_i$) | −10 (1%$_i$) |
| $\Delta E_{elstat}$ | −179 (55%$_a$) | −251 (51%$_a$) | −305 (48%$_a$) | −503 (29%$_a$) |
| $\Delta E_{orb}$ | −145 (45%$_a$) | −244 (49%$_a$) | −333 (52%$_a$) | −1230 (71%$_a$) |
| $\Delta E_{Pauli}$ | 230 | 310 | 394 | 774 |
| $\Delta E_{prep}$(Ads) | 9 | 33 | 60 | 547 |
| $\Delta E_{prep}$(surface) | 22 | 27 | 70 | 111 |

| HCl | (010) | (100) 2b | (100) 2b' | (011) | (101) |
|---|---|---|---|---|---|
| $\Delta E_{bond}^{VASP}$ | −41 | −99 | −86 | −93 | −311 |
| $\Delta E_{bond}$ | −42 | −97 | −83 | −90 | −306 |
| $\Delta E_{int}$ | −57 | −227 | −376 | −265 | −821 |
| $\Delta E_{disp}$ | −21 (36%$_i$) | −18 (8%$_i$) | −18 (5%$_i$) | −16 (6%$_i$) | −19 (2%$_i$) |
| $\Delta E_{elstat}$ | −106 (55%$_a$) | −313 (42%$_a$) | −445 (39%$_a$) | −328 (40%$_a$) | −466 (32%$_a$) |
| $\Delta E_{orb}$ | −88 (45%$_a$) | −436 (58%$_a$) | −708 (61%$_a$) | −484 (60%$_a$) | −1003 (68%$_a$) |
| $\Delta E_{Pauli}$ | 157 | 540 | 795 | 562 | 667 |
| $\Delta E_{prep}$(Ads) | 2 | 82 | 196 | 89 | 412 |
| $\Delta E_{prep}$(surface) | 13 | 48 | 96 | 86 | 102 |

| $H_2O$ | (010) | (100) | (011) | (101) |
|---|---|---|---|---|
| $\Delta E_{bond}^{VASP}$ | −85 | −92 | −114 | −113 |
| $\Delta E_{bond}$ | −86 | −93 | −114 | −111 |
| $\Delta E_{int}$ | −104 | −102 | −135 | −130 |
| $\Delta E_{disp}$ | −17 (16%$_i$) | −10 (10%$_i$) | −19 (14%$_i$) | −21 (16%$_i$) |
| $\Delta E_{elstat}$ | −199 (65%$_a$) | −153 (68%$_a$) | −219 (67%$_a$) | −221 (64%$_a$) |
| $\Delta E_{orb}$ | −108 (35%$_a$) | −72 (32%$_a$) | −107 (33%$_a$) | −123 (36%$_a$) |
| $\Delta E_{Pauli}$ | 220 | 133 | 210 | 235 |
| $\Delta E_{prep}$(Ads) | 1 | 2 | 1 | 1 |
| $\Delta E_{prep}$(surface) | 17 | 7 | 20 | 18 |

to a closed shell electronic structure inside VASP have been calculated with spatial orbitals inside AMS-BAND neglecting symmetry. Consequently, only the substoichiometric surfaces of (101) have been calculated with spin orbitals. Due to SCF convergence issues and to reduce computational time, these runs are performed utilizing symmetry at the good numerical quality yielding a SCF criterion of $1.6 \times 10^{-6}$ eV, as well as with an enforced ferromagnetic magnetic arrangement as found by VASP (see SI Section 3). Partial charges originate from the Charge Model 5 (CM5) scheme.[47,48] The NOCV deformation densities are plotted in AMSview and atomic structure visualizations are done in VESTA.[49]

## 3 | RESULTS AND DISCUSSION

### 3.1 | Strongest single adsorptions

The structure of the obtained strongest single adsorptions of each surface and adsorbate molecule are shown in Figure 3. Within each (*hkl*)·Ads, the strongest adsorption by $\Delta E_{bond}$ with relaxed reactants (Reaction R1) or $\Delta E_{int}$ with nonrelaxed reactant (Reaction R2) are obtained by the same structural isomer, with the exception of (100)·HCl, for which both structures are given. While the H-bond within the strongest adsorption by $\Delta E_{bond}$ (see Figure 3 **2b**) is formed to the

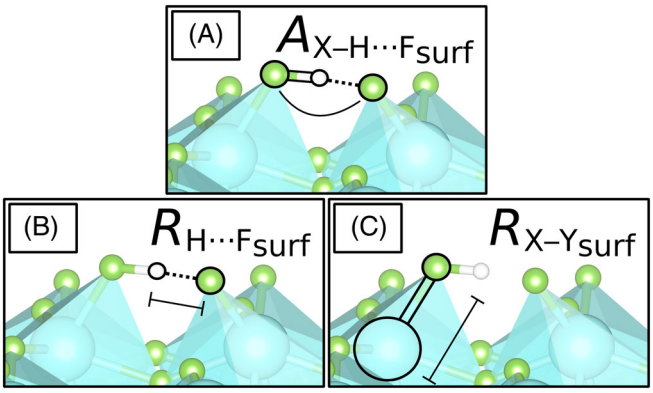


**FIGURE 4** Visualization of the analyzed structural adsorption parameters of H-bond angle ($A_{X-H\cdots F_{surf}}$, **A**) and distance ($R_{H\cdots F_{surf}}$, **B**), as well as direct O/F/Cl to $Y_{surf}$ coordination ($R_{X-Y_{surf}}$, **C**) on the example of the strongest bound (100)·HF.

neighboring surface polyhedron, the one with the strongest $\Delta E_{int}$ (**2b'**) is formed within the same polyhedron, which goes along with a much stronger H–Cl bond elongation.

In Table 1, their respective adsorption energies are related with the properties of the bare surface as $Y_{surf}$ accessibility, surface energy ($E_{surf}$), and ratio of that surface within a perfect nanocrystal at 0 K ($\%_{surf}$). It also gives the $Y_{surf}$ coordination numbers ($CN^{Y}_{surf}$) referring to the empty adsorption sites of the bare surfaces.

For (011) and (100), each direct coordination to a $Y_{surf}$ or H-bond to a $F_{surf}$ are formed to six-fold coordination polyhedra. A difference between the adsorbates is only found for the substoichiometric surface (101), for which $H_2O$ coordinates directly to an eight-fold coordinated $Y_{surf}$(III). On the other side, HF and HCl are bound to six-fold coordinated $Y_{surf}$ at a formal oxidation state of (II). These give the by far strongest $\Delta E_{int}$ as they dissociated in a hydride-forming manner discussed below. Comparing the adsorption of HF and HCl between the different surfaces, we find that $\Delta E_{bond}$ grows stronger with the $Y_{surf}$ accessibility. For $\Delta E_{int}$ the same relation is found for HCl adsorptions, while for HF, (011) and (100) swap positions. For $E_{surf}$ of the bare surfaces, no correlation to the most stable adsorptions is found. While (010) and (011) hardly differ in $E_{surf}$, the latter binds any adsorbate much stronger. On the contrary, the bare surface of (100) is significantly less stable but regardless of reactant relaxation, HF and HCl adsorb only slightly stronger onto (100) than (011). The opposite is even found for $H_2O$. Within $YF_3 \cdot H_2O$, the four surfaces seem to form two groups of slightly weaker (010) and (100) versus slightly stronger (011) and (101) interacting surfaces. However, these differences are much less pronounced than those found for $YF_3$·HF/HCl. A more detailed comparison of the strongest single adsorptions is given in Table 2 listing the different energy contributions to $\Delta E_{int}$ and $\Delta E_{bond}$.

$\Delta E_{disp}$ remains practically constant, while $\Delta E_{elstat}$ and $\Delta E_{orb}$ significantly vary and grow by $\Delta E_{int}$. The role of each of this three contributions is discussed in more detail for all adsorptions below. By $\Delta E_{orb}$, naturally also the counter-acting $\Delta E_{Pauli}$ grows. The listed $\Delta E_{prep}$ is foremost an indicator for the structural change within the reactant upon adsorption. Accordingly, it is largest by far for the hydride-forming adsorptions by HF and HCl onto substoichiometric (101). Within the nonhydride-forming adsorptions, $\Delta E_{prep}$ correlates with the change in adsorbate bond length due to the formed H-bond (see Figure 9 **3a**). Consequently, it is very low for the weaker adsorptions shown by $H_2O$, as well as those onto (010). By the [FHF]-like moiety forming HF adsorptions onto (100), $\Delta E_{prep}$ is almost half of the total $\Delta E_{bond}$. Finally, by the even stronger change in adsorbate bond length in (011)·HF and the respective HCl adsorptions onto (100) and (011), $\Delta E_{prep}$ is found to be larger than $\Delta E_{bond}$ itself. The largest ratio of $\Delta E_{prep}$ to $\Delta E_{bond}$ is found in (100)·HCl **2b'** with more than three times the latter.

## 3.2 | Structural features

For all adsorptions, the structural parameters for H-bond and direct coordinations are analyzed according to Figure 4. The results for single adsorbates versus $\Delta E_{int}$ are plotted in Figure 5. Practically equivalent trends are observed against $\Delta E_{elstat}$ or $\Delta E_{orb}$ (see Figures S18 and S19). The respective means over all surfaces weighted linearly by $\Delta E_{int}$ are also plotted. The Boltzmann weighted and nonweighted means within each or among all surfaces are listed in Table S2.

According to Jeffrey's classification,[50] H-bonds spanning an angle of 130–170° and/or measuring a distance of 150–220 pm may be considered moderately strong (see gray area in Figure 5A–B). Most $A_{X-H\cdots F_{surf}}$ and distances $R_{H\cdots F_{surf}}$ fall into this range. Strong H-bonds are found for HF and HCl adsorptions of about $|\Delta E_{int}| > 100$ kJ mol$^{-1}$ (see gray vertical line), while even the strongest bound $YF_3 \cdot H_2O$ only exhibit weak to moderate H-bonds. Taking a look at how these structural H-bonds parameters influence $\Delta E_{int}$, we find that the H-bond angle and more importantly its distance correlate with a stronger interaction for adsorptions of HF and HCl onto any surface (see Figure 5A–B). At comparable H-bond distances, $YF_3$·HF and $YF_3$·HCl, both give comparable $\Delta E_{int}$. However, as HCl is a much better H-donor than HF, the stronger bound $YF_3$·HCl form H-bonds of Cl···H–$F_{surf}$ yielding the shortest $R_{H\cdots F_{surf}}$ (see Figure 9 **3a**). Accordingly, these also come at the strongest $\Delta E_{int}$ giving a slightly (15 pm) lower weighted mean for HCl than HF adsorptions. On the contrary, the $YF_3 \cdot H_2O$ adsorptions show little variation and correlation. Only within (010), the dependence of $\Delta E_{int}$ onto the H-bond distance is clearly given. This already indicates, that the H-bond contributes less to the adsorption compared to those of HF and HCl.

In contrast to the H-bond distance, a shorter $R_{X-Y_{surf}}$ correlates to a stronger interaction for all three adsorbates (see Figure 5C). At similar distances, similar $\Delta E_{int}$ for $YF_3$·HF and $YF_3 \cdot H_2O$ are found, while the respective $YF_3$·HCl adsorptions show an about 50 pm larger distance due to the equally larger ionic radius.[21] As the hydride-forming adsorptions onto the electron-rich, substoichiometric (101) possess no H-bond, these are also not given in Figure 5A–B. The formed negatively charged hydride ($q_{CM5}$(H)= −0.2 e) bridges two $Y_{surf}$ atoms with $R_{H-Y_{surf}}$ = 208–220 pm. Moreover, by their large $\Delta E_{int}$ (see Figure 7D), their direct coordinations ($R_{F-Y_{surf}}$ = 200 pm, $R_{Cl-Y_{surf}}$ = 252 pm) are

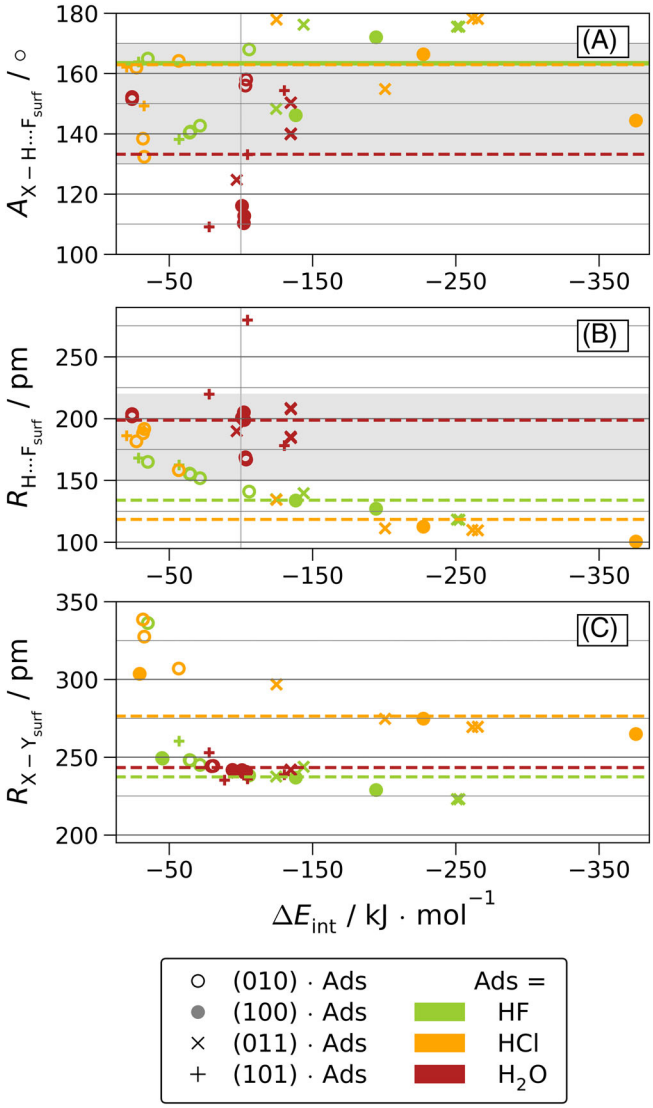


**FIGURE 5** Angles ($A_{X-H\cdots F_{surf}}$, **A**) and distances ($R_{H\cdots F_{surf}}$, **B**) of H-bond and direct O/F/Cl to $Y_{surf}$ coordinations ($R_{X-Y_{surf}}$, **C**) versus the interaction energy ($\Delta E_{int}$; PBE+D3(BJ)) for single nonhydride-forming adsorptions; the averages over all (*hkl*) weighted linearly by $\Delta E_{int}$ are also given (dashed lines).

also outside the zoomed window of Figure 5C. In the following, the hydride-forming adsorptions are labeled (101)·$H_{3Å}$F/Cl according to the relaxed interatomic distance of $R_{H-F/Cl} = 3$ Å of the dissociated adsorbate.

## 3.3 | Dispersion energy

The strength of dispersion is linked to the polarizability, which is especially low for fluorine. Therefore, the energy attributed to dispersion interaction is low but increases as $YF_3 \cdot HF < YF_3 \cdot H_2O < YF_3 \cdot HCl$ (see Figure 6A). It only contributes < 10% to the sum of attractive interactions and $\Delta E_{disp}$ (see Equation 5 and Figure 6B). Even for very weak $\Delta E_{int}$ and thus also weak electrostatics and orbital interactions,

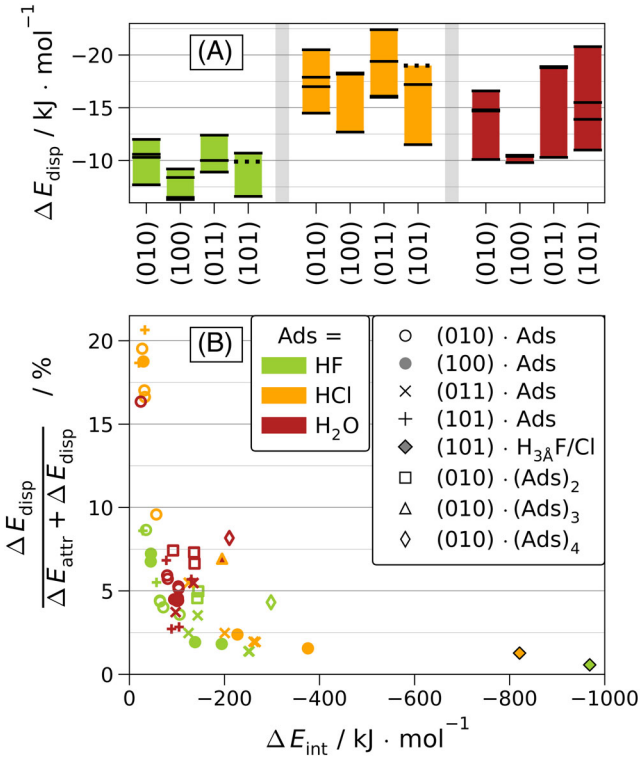


**FIGURE 6** Ranges of dispersion energy determined with PBE+D3(BJ) ($\Delta E_{disp}$, **A**) per surface (*hkl*) for all single adsorptions. The individual values are marked by black bars or dotted bars for the hydride-forming structures of (101)·$H_{3Å}$F/Cl. Ratio of $\Delta E_{disp}$ within the sum of $\Delta E_{disp}$ and attractive energies ($\Delta E_{attr}$, **B**) versus the interaction energy ($\Delta E_{int}$) for all surfaces and adsorbates.

dispersion accounts for only a fifth of the adsorption. The relation of $\Delta E_{disp}$ versus $\Delta E_{int}$ is plotted in Figure S20.

## 3.4 | Electrostatic and orbital contributions in single adsorptions

As discussed above, $\Delta E_{int}$ is only little effected by dispersion. The significant contributions originate from electrostatics and orbital interactions. Their ranges within each surface are plotted together with the adsorption energies in Figure 7. As this study did not sample the conformational space in its entirety, but focused on the adsorption sites of strongest interactions, the plotted ranges rather visualize the limit of strongest energy contributions. We expect that a more complete scan of the conformational space would include very weak adsorptions with near zero energies for any of these ranges.

Extremely large energy ranges are observed for (101)·HF/HCl due to the very strong hydride-forming adsorptions on one side and very weak adsorptions otherwise. On the contrary, $YF_3 \cdot H_2O$ adsorptions are rather insensitive to the surface and the overall $\Delta E_{int}$ or $\Delta E_{bond}$ hardly differ between the four surfaces. Within each (*hkl*)·Ads, the conformation with the strongest $\Delta E_{int}$ also shows the strongest $\Delta E_{elstat}$, as well as $\Delta E_{orb}$ with the exception of (101)·$H_2O$. Comparing the strongest (Figure 3 **4c**) and second strongest interacting

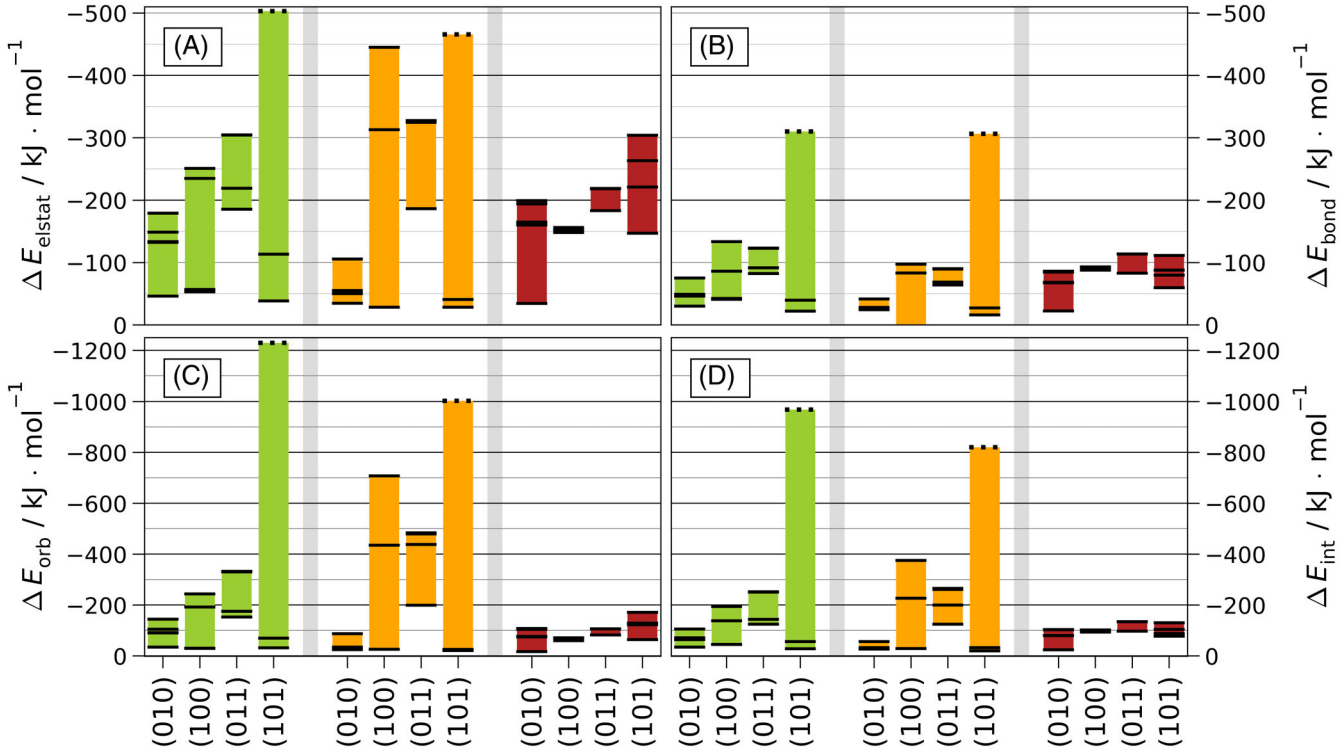


**FIGURE 7** Ranges of electrostatic energy ($\Delta E_{elstat}$, **A**), bonding energy ($\Delta E_{bond}$, B), orbital energy ($\Delta E_{orb}$, **C**), and interaction energy ($\Delta E_{int}$, **D**) per surface (*hkl*) for all single adsorptions of $YF_3$·HF (green), $YF_3$·HCl (orange), and $YF_3 \cdot H_2O$ (red). The individual values are marked by black bars or dotted bars for the hydride-forming structures of (101)· $H_{3Å}$F/Cl.

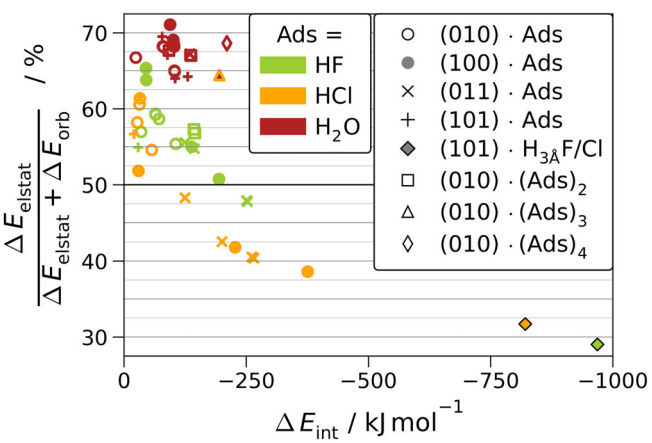


**FIGURE 8** Ratio of electrostatic energy ($\Delta E_{elstat}$; PBE+D3(BJ)) within the attractive energies ($\Delta E_{attr}$) versus the interaction energy ($\Delta E_{int}$) for all adsorptions.

structures, the latter is by about 40 kJ mol$^{-1}$ weaker in $\Delta E_{int}$, but stronger by the same magnitude in each of $\Delta E_{elstat}$ and $\Delta E_{orb}$. This goes along with a considerable shift in electron density at $Y_{surf}$ only found in the latter structure ($\Delta q_{Bader}$(Y)= +0.4 e).[32] However, by the significant shift in electronic density, the repulsive $\Delta E_{Pauli}$ is also considerably larger and overcompensates the gains in electrostatic and orbital interactions. The ratio of $\Delta E_{elstat}$ within $\Delta E_{attr}$, the sum of $\Delta E_{elstat}$ and $\Delta E_{orb}$ (see Equation 5) is visualized in Figure 8. Depending on which term dominates within this ratio, an adsorption may classify as ionic or covalent. For $YF_3$·HF and $YF_3$·HCl adsorptions of at least $|\Delta E_{int}| \geq 60$ kJ mol$^{-1}$, for which the weak contribution of $\Delta E_{disp}$ becomes negligible, $\Delta E_{int}$ grows stronger with the degree of covalency. This correlation is not found for $YF_3 \cdot H_2O$, for which electrostatics strongly dominate the interaction regardless of $\Delta E_{int}$. The ionic versus covalent bonding character described for the single molecule adsorption remain the same for the simultaneous adsorption of multiple molecules. $\Delta E_{int}$ per adsorbate molecule is also not significantly altered up to the maximum tested number of $YF_3$·$(Ads)_4$.

Within the nonhydride-forming adsorptions, the increase in covalent bonding character correlates with the formation of strong H-bonds to $F_{surf}$ introduced above (see Figure 5). For $YF_3$·HF, it is the formation of rather symmetric [FHF] moieties (see Figure 3 **2–3a**). For $YF_3$·HCl, it is the partial dissociation of H–Cl to form a H-bond of Cl···H – $F_{surf}$ (see Figure 3 **2b'**+**3b** and Figure 9 **3a**). Alike, structural features that come with dominating electrostatics are weak or even absent H-bonds. Instead, the adsorption is dominated by a direct coordinated via X–$Y_{surf}$ with X = {O, F, Cl}. This supports that the direct coordination to $Y_{surf}$ is electrostatic dominated, while the H-bond to $F_{surf}$ is orbital dominated.

## 3.5 | Pairwise electron interactions

The orbital energy is further divided into pairwise NOCV interactions between surface and adsorbate. All corresponding deformation densities are considered, which show an electronic charge displacement

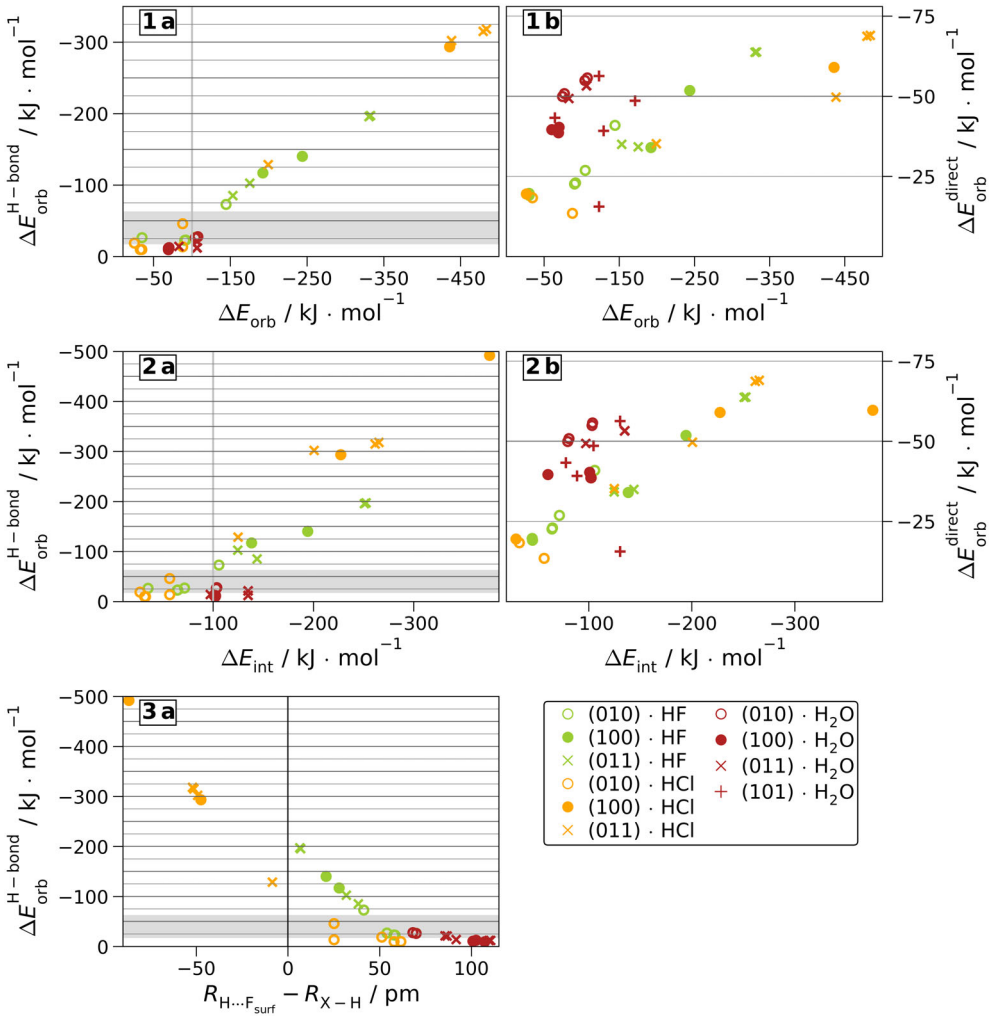


**FIGURE 9** PBE+D3(BJ) energies of H-bonds to $F_{surf}$ ($\Delta E_{orb}^{H\text{-bond}}$, **a**) or direct coordinations to $Y_{surf}$ ($\Delta E_{orb}^{direct}$, **b**) versus the orbital energy ($\Delta E_{orb}$; **1a–b**), interaction energy ($\Delta E_{int}$; **2a–b**) or the difference of H-bond and adsorbate bond length ($R_{H\cdots F_{surf}} - R_{X-H}$, **3a**) with X = {O, F, Cl} for all nonhydride-forming single adsorptions.

upon adsorption of $\nu_n \geq 0.1$ e. This relatively low cutoff is chosen as the overall $\Delta E_{orb}$ within many $YF_3$·Ads, and thus, also their $\nu_n$, are rather small. All $\nu_n$ versus their corresponding contribution to the orbital energy ($\Delta E_{orb}^n$) are plotted in Figure S21. The flatter slope of $\Delta\nu_n/\Delta E_{orb}^n$ shown by the stronger adsorbed HF or HCl onto (100), (011) or (101) also supports that their bonding character is less ionic than within the weaker adsorbed (*hkl*)·Ads. The NOCV deformation densities are grouped into different interactions of $\sigma$-like or $\pi$-like interactions of three-centered H-bonds of X–H···$F_{surf}$ (or X···H – $F_{surf}$) in contrast to two-centered direct coordinations of X–$Y_{surf}$ with X = {O, F, Cl} or H – $F_{surf}$. However, only the $\sigma$-like X–H···$F_{surf}$ and $\sigma$-like X–$Y_{surf}$ are found within most $YF_3$·Ads. These two interactions also give the largest $\nu_n$ for all nonhydride-forming adsorptions. Their $\Delta E_{orb}^n$ are plotted in Figure 9 versus the overall $\Delta E_{orb}$ or $\Delta E_{int}$ (for the corresponding $\nu_n$ see Figure S23). Note that within the former (**1a–b**), the strongest bound (100)·HCl by $\Delta E_{int}$ (**2b'**) is outside the zoom because of its very large $\Delta E_{orb}$ (see Table 2). Its deformation densities are discussed versus the strongest bound (100)·HCl by $\Delta E_{bond}$ (**2b**) in the SI (see Figure S24). The same applies to the hydride-forming adsorptions of (101)·$H_{3Å}$F/Cl (see Figure S25). On the opposite, weak end of the $\Delta E_{int}$ range, several H-bonds and direct coordinations found by atomic positions (see Figure 5) are too weak in their pairwise electron interaction to meet the applied threshold. This is most prominently the case within the weak, nonhydride-forming adsorptions onto (101), for which no H-bond, but only the direct coordinations of (101)·$H_2O$ show. For these, the sum of α and β-components are plotted.

Moderate H-bonds are defined to be bound by 17–63 kJ mol$^{-1}$ (see gray area in Figure 9 **1–3a**).[50] Thus, $YF_3$·HF/HCl adsorptions with an interaction energy stronger than −100 kJ mol$^{-1}$ possess H-bonds classifying as strong by their $\Delta E_{orb}^{H\text{-bond}}$. This energy agrees excellently with the criteria on H-bond distances $R_{X-H\cdots F}$ (see gray line in Figure 5A–B). For the H-bond strength, we find a strong dependence on the surface by HF and even more so by HCl, but practically none for $H_2O$. For the latter, all H-bonds are much weaker than those formed by HF or HCl. Among the adsorbates, the increasing H-bond strength can be ordered as (*hkl*)·$H_2O$ < (*hkl*)·HF < (*hkl*)·HCl for all (*hkl*) but (010), for which the strongest bound (010)·HF possess a 27 kJ >mol$^{-1}$ stronger $\Delta E_{orb}^{H\text{-bond}}$ than (010)·HCl. However, the fluorine-rich surface of (010) shows the smallest differences between the adsorbates, as well as the smallest overall $\Delta E_{orb}^{H\text{-bond}}$. Note that these trends observed for the H-bond strength support the findings on the maximum adsorption strengths and ionic versus covalent adsorption character discussed

above. We therefore conclude that the formation of strong H-bonds sets the interaction of $YF_3$ towards HF and HCl apart from $H_2O$. Coming to the electrostatic-driven direct coordinations, we find that the total ranges of $\Delta E_{orb}^{direct}$ are much smaller than the corresponding H-bond terms (see Figure 9 **2a–b**). Accordingly, the direct coordination strength is less decisive for the bonding than the H-bond strength for the moderately and strongly bound $YF_3$·HF/HCl. On the contrary, it is more decisive than the H-bond strength for $YF_3 \cdot H_2O$. For a detailed look at the bonding patterns, it should be noted that several weakly, but also moderately ($|\Delta E_{int}| < 95$ kJ mol$^{-1}$) bound adsorbates coordinate via the direct X–$Y_{surf}$ only, whereas a few weakly ($|\Delta E_{int}| < 35$ kJ mol$^{-1}$) coordinations coordinate by the H-bond only. Furthermore, within some weakly and moderately bound (*hkl*)·HF/HCl, NOCV deformation densities are found that show a combination of X–H···$F_{surf}$ and X–$Y_{surf}$. Therefore, the corresponding energy contributions were chosen to be halved to enter each of the categories. From these, only within one (010)·HCl, both $\nu_n$ remain above the threshold and are thus also present as two entries at the same overall $\Delta E_{orb}$ or $\Delta E_{int}$. The only actual, although weak bifurcated H-bond is found for the strongest adsorbed (011)·$H_2O$ ($\Delta E_{int} = -135$ kJ mol$^{-1}$) with $\Delta E_{orb}^{H\text{-bond}} = -\{12,21\}$ kJ mol$^{-1}$ (see Figure 3 **3c**). The dependency of H-bond energy to the difference in H-bond and adsorbate bond length is shown in Figure 9 **3a**. Equivalent plots for the eigenvalues and the overall orbital energy are given in Figure S22. For the moderate and strong H-bonds, the H-bond strength increases linearly with a decreasing $R_{H-F_{surf}} - R_{X-H}$. The strongest H-bond formed by HF is found for (011)·HF forming a [FHF] moiety (see Figure 10 **1a**). Before adsorption, the $F_{surf}$ is bridging two six-fold coordinated $Y_{surf}$. Upon HF adsorption, this bridge is elongated to a [FHF] leaving the $Y_{surf}$ coordination number unchanged. The [FHF] angle is almost linear and the two $R_{H-F}$ differ by only 6 pm among each other and are very close to the symmetric H–F lengths of 114 pm within gaseous $[FHF]^-$.[51,52] Because the H–F interaction is much stronger than the respective H–Cl one, or in other words, because HF is the worse H-bond donor, the strongest H-bonds within $YF_3$·HCl are of Cl···H – $F_{surf}$ type, in which the hydrogen is much closer to $F_{surf}$ (see Figure 10 **1b**). Within (011)·HCl, the H-bond is about 120 kJ mol$^{-1}$ stronger than within the respective HF structure (see Figure 10 **2a–b**).

At the same time, the direct coordinations of Cl–$Y_{surf}$ and F–$Y_{surf}$ are very similar in $\Delta E_{orb}^{direct}$ (see Figure 10 **3a–b**). However, the NOCV deformation density predominantly attributed to F – $Y_{surf}$ also accumulates electron density along H – $F_{surf}$. Noteworthy is also the third main contribution of the two adsorptions, which favors Cl···H – $F_{surf}$ by another 20 kJ mol$^{-1}$ over F – H – $F_{surf}$ (see Figure 10 **4a–b**). A very similar energy difference reproduces itself also in $\Delta E_{elstat}$. On the other hand, the H-bond-driven much larger $\Delta E_{orb}$ of (011)·HCl is counter-balanced by $\Delta E_{Pauli}$ leaving an overall difference of merely about 10 kJ mol$^{-1}$ within $\Delta E_{int}$ (see Table 2). Finally, due to the large $\Delta E_{prep}$ required for the partial H–Cl dissociation, the (011)·HCl adsorption is even about 30 kJ mol$^{-1}$ weaker judged by $\Delta E_{bond}$.

Among all studied adsorptions, the largest $\Delta E_{orb}$, as well as overall $\Delta E_{int}$ is shown by (101)·$H_{3Å}$F/Cl, which spontaneously dissociated in a hydride-forming possess. This is accompanied by a reduction in magnetic moment from eight to six. At the bare substoichiometric surface, all formal 8 Y(II) centers orientate ferromagnetically. However, within (101)·$H_{3Å}$F/Cl, the Y-centers coordinated by the anions lost their magnetic moment. Something that is not observed for weakly bound (101)·HF/Cl or the (101)·$H_2O$. The classification as charge transfer is backed up by the change in electron density topography leading to the change in partial Bader charges.[32] The Löwdin-based CM5 partial charges are smaller in magnitude but qualitatively agree. These show a reduction from ±0.2 e in free HF or ±0.1 e in free HCl to $q_H = -0.2$ e, $q_F = -0.5$ e or $q_{Cl} = -0.4$ e for (101)·$H_{3Å}$F/Cl. The dissociated atoms coordinate to the same polyhedron (see Figure 3 **4a–4b**). Nonetheless, in contrast to the H-bond partially dissociated adsorbates (see negative distance differences of (100)/(011)·HCl in Figure 9), within in this hydride-forming dissociation, the two anions are almost 1 Å further apart with $R_{H-F} = 2.57$ Å or $R_{H-Cl} = 2.85$ Å versus for example, $R_{H-Cl} = 1.87$ Å in (100)·HCl. Their spin-asymmetric NOCV deformation densities are visualized in Figure 11 using arabic labels for (101)·$H_{3Å}$F and roman labels for (101)·$H_{3Å}$Cl.

The deformation densities of both adsorptions are equivalent in shape. However, due to the smaller electronegativity of Cl and therefore less ionic character of the (101)·$H_{3Å}$Cl adsorption (see Figure 8), the respective $\Delta E_{orb}^{n}$ are smaller than those of (101)·$H_{3Å}$F. This is especially pronounced (23%) for the strongest $\Delta E_{orb}^{\alpha}$ (**2a**, **IIa**). It corresponds to one transferred α-electron previously rather localized at $Y_{surf}$ towards H and F or Cl spanning a larger volume as typical for anions. By the second strongest interaction (**2b**, **IIb**), β-electron

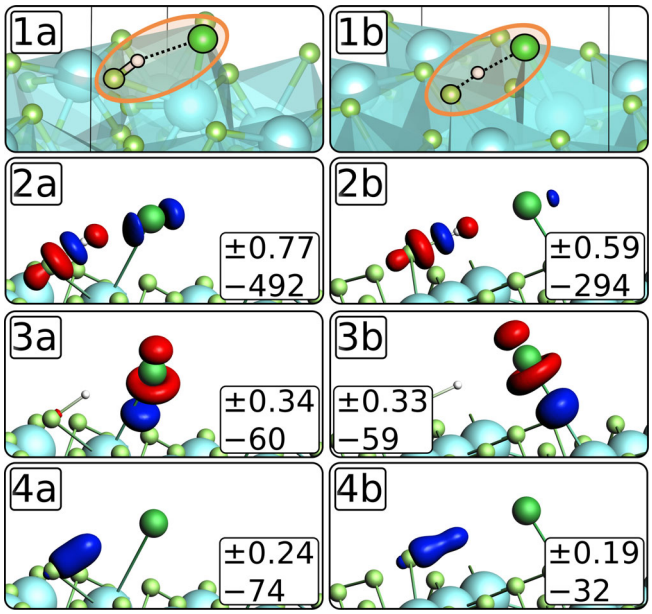


**FIGURE 10** Strongest adsorbed structures within (011)·HF (**1a**) and (011)·HCl (**1b**), with respective NOCV deformation densities (red = reduction / blue = accumulation of electron density) of $|\Delta E_{orb}^{n}| > 20$ kJ mol$^{-1}$ visualized with isosurface values of 0.006 (**2a–b**), 0.0015 (**3a–b**), and 0.0003 (**4a–4b**). Within the inserts, the first row gives the eigenvalues ($\nu_n$) in e and the each second row the $\Delta E_{orb}^{n}$ in kJ mol$^{-1}$.

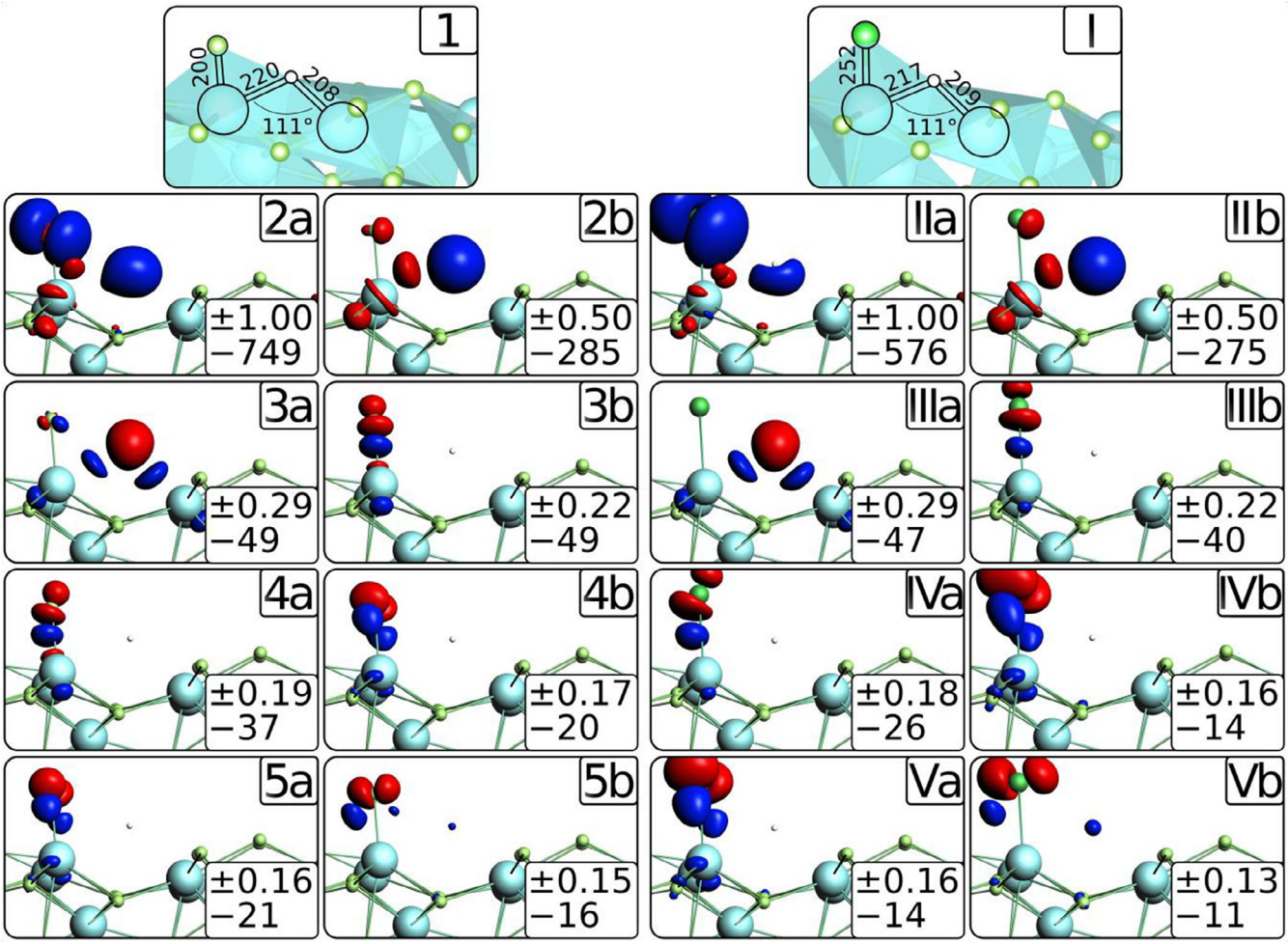


**FIGURE 11** Strongest adsorbed structures of (101)·$H_{3Å}F$ (**1**) and (101)·$H_{3Å}Cl$ (**I**) with respective NOCV deformation densities (**2**–**5**, **II**–**V**) for α (**a**) and β-spin components (**b**) visualized with isosurface values of 0.0035 (**2a**, **IIa**), 0.0030 (**2b**, **IIb**), 0.0015 (**3b**, **IIIb**), 0.0010 (**3**–**4a**, **IIIa**), 0.0007 (**IVa**), 0.0004 (**4b**, **5a**–**b**), and 0.0002 (**IVb**, **Va**–**b**). Within the inserts, the first row gives the eigenvalues ($\nu_n$) in e and the second row the $\Delta E^n_{orb}$ in kJ mol$^{-1}$.

density of 0.5 e further accumulates at H, while along the same directions 0.3 e of α-electron density depletes from H (**3a**, **IIIa**). The next weaker interactions show the same $\sigma$-like direct coordination of F – $Y_{surf}$ (**4a**–**b**) and Cl–$Y_{surf}$ (**IVa**–**b**) with a comparable $\nu_{direct}$ and $\Delta E_{orb,direct}$ as within the nonhydride-forming $YF_3$·Ads (see Figure 10 **3a**–**b**). The weaker contributions are $\pi$-like direct coordinations of F – $Y_{surf}$ (**4b**, **5a**–**b**) or Cl – $Y_{surf}$ (**IVb**, **Va**–**b**). In accordance to the negative polarization of H, no deformation density indicates an H-bond.

## 4 | CONCLUSIONS

Four surfaces, (010), (100), (011), and (101) of β-$YF_3$ have been studied for their binding affinity and chemisorption bonding patterns towards HF, HCl, and $H_2O$. Applying density functional theory with periodic energy decomposition and natural orbital for chemical valence analysis, the adsorption energies were quantified according to their subcomponents. We found that the $H_2O$ adsorptions are strongly ionic with electrostatics constituting about 65% of all attractive forces for practically any surface and adsorption energy. As a result, we find a very low sensitivity towards the surface termination. This is accompanied by a bonding pattern dominated by the O – $Y_{surf}$ coordination. On the other hand, the adsorptions of HF and HCl show a varying electrostatic ratio from 30% to 60% between and within the different surfaces. We find a correlation of an increasing H-bond strength with a growing covalent bonding character and growing adsorption strength. These adsorptions are therefore highly sensitive to the surface termination and show a large range within the interaction energy. H-bonds with similar distances give comparable interaction, electrostatic, and orbital interaction energies. For HF, the strongest H-bonds are the most symmetric F – H – $F_{surf}$. Overall, the strongest H-bonds and thus most covalent adsorptions of Cl···H – $F_{surf}$ are formed by HCl due to its better quality as H-donor. However, including the relaxation of the reactants, each surface favors the adsorption of HF over HCl. These findings reproduce the reported higher affinity of Y(III) solutions towards fluoride over chloride. No change in bonding patterns has been found upon the co-adsorption of up to four adsorbates.

## ACKNOWLEDGMENTS

The authors thank the North-German Supercomputing Alliance (Norddeutscher Verbund zur Förderung des Hoch-und Höchstleistungsrechnens HLRN) and the Zentraleinrichtung für Datenverarbeitung (ZEDAT) at the Freie Universität Berlin for computational resources and the German Science Foundation (DFG) for funding (Project-ID 387284271) within the CRC 1349—Fluorine-Specific Interactions. Open Access funding enabled and organized by Projekt DEAL.

## DATA AVAILABILITY STATEMENT

All surface structures relaxed within VASP are available within the NOMAD repository (ID: xoipefEvRGOWfNVSx_R1MA). All electronic structures obtained within AMS-BAND are available at ZENODO (https://doi.org/10.5281/zenodo.7784827; https://doi.org/10.5281/zenodo.7788901; https://doi.org/10.5281/zenodo.7788977; https://doi.org/10.5281/zenodo.7789104; https://doi.org/10.5281/zenodo.7789115). Further data can be requested from the authors.

## ORCID

*Jennifer Anders* https://orcid.org/0000-0001-6941-2001
*Florian Kreuter* https://orcid.org/0000-0001-5938-9071
*Ralf Tonner-Zech* https://orcid.org/0000-0002-6759-8559
*Beate Paulus* https://orcid.org/0000-0002-9834-4949

## REFERENCES

[1] M. Bau, P. Dulski, *Contrib. Mineral. Petrol.* **1995**, *119*, 213.
[2] M. Bau, *Contrib. Mineral. Petrol.* **1996**, *123*, 323.
[3] A. A. Migdisov, A. E. Williams-Jones, T. Wagner, *Geochim. Cosmochim. Acta* **2009**, *73*, 7087.
[4] A. Loges, A. A. Migdisov, T. Wagner, A. E. Williams-Jones, G. Markl, *Geochim. Cosmochim. Acta* **2013**, *123*, 403.
[5] J. Stefanski, S. Jahn, *Solid Earth* **2020**, *11*, 767, https://se.copernicus.org/articles/11/767/2020/se-11-767-2020.pdf
[6] Q. Guan, Y. Mei, B. Etschmann, D. Testemale, M. Louvel, J. Brugger, *Geochim. Cosmochim. Acta* **2020**, *281*, 168.
[7] Q. Guan, Y. Mei, B. Etschmann, M. Louvel, D. Testemale, R. Spezia, J. Brugger, *Geochim. Cosmochim. Acta* **2022**, *330*, 27.
[8] M. R. Payne, A. P. Gysi, N. C. Hurtig, *Chem. Geol.* **2023**, *617*, 121256.
[9] D. Atencio, A. C. Bastos Neto, V. P. Pereira, J. T. M. M. Ferron, M. Hoshino, T. Moriyama, Y. Watanabe, R. Miyawaki, J. M. V. Coutinho, M. B. Andrade, et al., *Mineral. Mag.* **2015**, *79*, 767.
[10] A. Zalkin, D. H. Templeton, *J. Am. Chem. Soc.* **1953**, *75*, 2453.
[11] V. Pankratov, M. Kirm, H. von Seggern, *J. Lumin.* **2005**, *113*, 143, http://www.sciencedirect.com/science/article/pii/S0022231304004351
[12] A. Kaminski, *Laser Crystals: Their Physics and Properties*, 2nd ed., Springer, Berlin **1990**. https://doi.org/10.1007/978-3-540-70749-3
[13] Z. Kollia, E. Sarantopoulou, A. C. Cefalas, C. A. Nicolaides, A. K. Naumov, V. V. Semashko, R. Y. Abdulsabirov, S. L. Korableva, M. A. Dubinskii, *J. Opt. Soc. Am. B* **1995**, *12*, 782, http://josab.osa.org/abstract.cfm?URI=josab-12-5-782
[14] E. Sarantopoulou, Z. Kollia, A. C. Cefalas, *Opt. Mater.* **2001**, *18*, 23, http://www.sciencedirect.com/science/article/pii/S0925346701001240
[15] M. M. Lage, A. Righi, F. M. Matinaga, J.-Y. Gesland, R. L. Moreira, *J. Phys.: Condens. Matter* **2004**, *16*, 3207, https://iopscience.iop.org/article/10.1088/0953-8984/16/18/021
[16] M. O'Keeffe, *Science* **1973**, *180*, 1276.
[17] Y. V. Pogorenko, R. M. Pshenychnyi, V. I. Lutsyk, A. O. Omel'chuk, *IOP Conf. Sci. Eng.* **2017**, *175*, 012039.
[18] P. P. Fedorov, N. I. Sorokin, *Inorg. Mater.* **2017**, *53*, 1307.
[19] X. Cui, T. Hu, J. Wang, J. Zhang, X. Zhong, Y. Chen, X. Li, J. Yang, C. Gao, *Nanomaterials* **2018**, *8*, 995.
[20] X. Dai, Y. Komatsu, R. Shimizu, T. Hitosugi, *Appl. Phys. Express* **2020**, *13*, 85507, https://doi.org/10.35848/1882-0786/aba22d
[21] R. D. Shannon, *Acta Cryst. A* **1976**, *32*, 751.
[22] K. Hans Wedepohl, *Geochim. Cosmochim. Acta* **1995**, *59*, 1217, https://www.sciencedirect.com/science/article/pii/0016703795000382
[23] A. A. Yaroshevsky, *Geochemistry Int.* **2006**, *44*, 48.
[24] A. Loges, A. A. Migdisov, T. Wagner, A. E. Williams-Jones, G. Markl. Proceedings of the 22nd Goldschmidt Conference, Montréal, QC, Canada, 24–29 June 2012, The Mineralogical Society, 2013.
[25] W. Zhang, T. Yan, *J. Mol. Liq.* **2022**, *347*, 118367https://www.sciencedirect.com/science/article/pii/S0167732221030920
[26] K. Newcomb, S. P. Tiwari, N. Rai, E. J. Maginn, *Phys. Chem. Chem. Phys.* **2018**, *20*, 15753.
[27] G. P. Shironosova, I. R. Prokopyev, *Engineering* **2019**, *330*, 7.
[28] F. H. Spedding, D. C. Henderson, *J. Chem. Phys.* **1971**, *54*, 2476.
[29] J. Anders, N. Limberg, B. Paulus, *Materials* **2022**, *15*, 6048.
[30] G. Wulff, *Z. Kristallogr. Cryst. Mater.* **1901**, *34*, 449.
[31] M. V. Laue, Z Kristallogr, *Materials* **1943**, *105*, 124.
[32] J. Anders, H. Wiedenhaupt, B. Paulus, *Crystals* **2023**, *13*, 555.
[33] S. Grimme, J. Antony, S. Ehrlich, H. Krieg, *J. Chem. Phys.* **2010**, *132*, 154104.
[34] K. Kitaura, K. Morokuma, *Int. J. Quantum Chem.* **1976**, *10*, 325.
[35] T. Ziegler, A. Rauk, *Theor. Chim. Acta* **1977**, *46*, 1.
[36] M. Raupach, R. Tonner, *J. Chem. Phys.* **2015**, *142*, 194105.
[37] M. P. Mitoraj, A. Michalak, T. Ziegler, *J. Chem. Theory Comput.* **2009**, *5*, 962.
[38] L. Pecher, R. Tonner, *Wiley Interdiscip. Rev. Comput. Mol. Sci.* **2019**, *9*, 1759.
[39] G. Kresse, J. Hafner, *J. Phys.: Condens. Matter* **1994**, *6*, 8245.
[40] J. P. Perdew, K. Burke, M. Ernzerhof, *Phys. Rev. Lett.* **1996**, *77*, 3865, https://link.aps.org/doi/10.1103/PhysRevLett.77.3865
[41] P. E. Blöchl, *Phys. Rev. B* **1994**, *50*, 17953, https://link.aps.org/doi/10.1103/PhysRevB.50.17953
[42] G. Kresse, D. Joubert, *Phys. Rev. B* **1999**, *59*, 1758, https://link.aps.org/doi/10.1103/PhysRevB.59.1758
[43] S. Grimme, S. Ehrlich, L. Goerigk, *J. Comput. Chem.* **2011**, *32*, 1456.
[44] BAND, *SCM, Theoretical Chemistry*, Vrije Universiteit, Amsterdam, The Netherlands **2021**, http://www.scm.com
[45] E. Van Lenthe, E. J. Baerends, *J. Comput. Chem.* **2003**, *24*, 1142.
[46] P. H. T. Philipsen, E. van Lenthe, J. G. Snijders, E. J. Baerends, *Phys. Rev. B* **1997**, *56*, 13556, https://link.aps.org/doi/10.1103/PhysRevB.56.13556
[47] A. V. Marenich, S. V. Jerome, C. J. Cramer, D. G. Truhlar, *J. Chem. Theory Comput.* **2012**, *8*, 527.
[48] C. A. Peeples, G. Schreckenbach, *J. Chem. Theory Comput.* **2016**, *12*, 4033.
[49] K. Momma, F. Izumi, *J. Appl. Crystallogr.* **2011**, *44*, 1272.
[50] G. Jeffrey, *An Introduction to Hydrogen Bonding*, Oxford University Press, New York, Oxford **1997**.
[51] J. W. Larson, T. B. McMahon, *Inorg. Chem.* **1984**, *23*, 2029.
[52] S. Gronert, *J. Am. Chem. Soc.* **1993**, *115*, 10258.

## SUPPORTING INFORMATION

Additional supporting information can be found online in the Supporting Information section at the end of this article.

**How to cite this article:** J. Anders, H. Wiedenhaupt, F. Kreuter, R. Tonner-Zech, B. Paulus, *J. Comput. Chem.* **2023**, *44*(25), 1986. https://doi.org/10.1002/jcc.27168